

Thermal relaxation in metal films limited by diffuson lattice excitations of amorphous substrates

Elmira M. Baeva, Gregory N. Goltsman, and Anna I. Kardakova

*Moscow Pedagogical State University, 29 Malaya Pirogovskaya Street, Moscow, Russia and
National Research University Higher School of Economics, 20 Myasnitskaya Street, Moscow, Russia*

Nadezhda A. Titova

Moscow Pedagogical State University, 29 Malaya Pirogovskaya Street, Moscow, Russia

Louis Veyrat and Benjamin Sacépé

Université Grenoble Alpes, CNRS, Grenoble INP, Institut Néel, 38000 Grenoble, France

Alexander V. Semenov

*Moscow Pedagogical State University, 29 Malaya Pirogovskaya Street, Moscow, Russia and
Moscow Institute of Physics and Technology, 9 Institutsky Lane, Dolgoprudny, Russia*

Vadim S. Khrapai

*National Research University Higher School of Economics, 20 Myasnitskaya Street, Moscow, Russia and
Institute of Solid State Physics, Russian Academy of Sciences, Chernogolovka, Russia*

Here we examine the role of the silicon-based amorphous insulating substrate in the thermal relaxation in thin NbN, InO_x, and Au/Ni films at temperatures above 5 K. The studied samples are made up of metal bridges on an amorphous insulating layer lying on or suspended above a crystalline substrate. Noise thermometry was used to measure the electron temperature T_e of the films as a function of Joule power per unit of area P_{2D} . In all samples, we observe the dependence $P_{2D} \propto T_e^n$ with the exponent $n \simeq 2$, which is inconsistent with both electron-phonon coupling and Kapitza thermal resistance. In suspended samples, the functional dependence of $P_{2D}(T_e)$ on the length of the amorphous insulating layer is consistent with the linear T -dependence of the thermal conductivity, which is related to lattice excitations (diffusons) for the phonon mean free path smaller than the dominant phonon wavelength. Our findings are important for understanding the operation of devices embedded in amorphous dielectrics.

I. INTRODUCTION

Dielectric substrates covered with an amorphous insulator are often used as a platform for planar electronic devices. The use of an amorphous insulating layer (AIL) in electronic circuits provides technological advantages for optical circuits [1–3] or electrostatically gated devices [4, 5] or fabrication of amorphous metallic films used in single-photon detectors [6, 7], calorimeters [8], and superconducting resonators [9, 10]. In the latter case, materials have greater robustness with respect to the structural defects. An AIL further ensures a greater yield of practical devices and uniformity of their characteristics [11]. Substrates with an AIL are also commonly used by default for the fabrication of strongly disordered superconducting films, which are of interest for the study of superconductor-insulator transition [12, 13]. Despite the obvious technological advantages, amorphous materials also cause some undesirable effects in device operations. For instance, in resonators and qubits, two-level systems located in amorphous media lead to energy dissipation and decoherence at low temperatures [14]. In electromagnetic detectors, enclosed in an amorphous dielectric, additional phonon bottlenecks in thermal relaxation are

observed [15–17], which restrict the response timing of the devices. This is manifested in the fact that the magnitude of the phonon escape time τ_{esc} is much greater than the typical ballistic phonon time of flight d/v_s [18], where v_s and d are the sound velocity and metal-film thickness, respectively. The observation is now interpreted in terms of strong reflection anisotropy of ballistic phonon at the interface depending on the angle of incidence [16, 19, 20].

To understand the thermal behavior of thin-film devices, we conduct a systematic study of the electronic heat flow rate, which is proportional to the power-law dependence $P_{2D} \propto T_e^n - T_b^n$, where T_e and T_b are the temperatures of electrons and the bath. Here, the exponent n provides information on the dominant energy-relaxation mechanism. At low temperature T , electron-phonon coupling usually mediates the heat flow rate, and in this case, n ranges from 4 to 6 [8]. However, in devices on amorphous dielectric substrates, sometimes smaller values of n are observed at low T [21]. This fact cannot be captured by conventional models for electron-phonon coupling.

Heat transfer in amorphous systems is fundamentally different from that in crystalline materials. Above all, the phonon propagation in disordered media is mainly

diffusive, since the phonon mean free path (l_{ph}) is limited by scattering at defects, boundaries, or two-level systems [22, 23]. In amorphous insulators, l_{ph} , which defines the thermal conductivity, is dependent on the phonon energy and strongly decreases with increase of T [24]. On reaching the Ioffe-Regel threshold, which corresponds to $l_{ph} \approx \lambda/2$, where λ is the dominant thermal phonon wavelength, phonons fade quickly, and the heat transfer is implemented by other vibrational excitations, known as diffusons [23, 25–27]. As a result, even a thin layer of an amorphous insulator between the metal film and the crystalline substrate can play a crucial role in the thermal transport in real devices. However, this effect is usually not taken into account in modern electrothermal models [28], which successfully describe single-photon detectors on polycrystalline materials [29] but poorly apply to devices embedded in an amorphous insulator [30, 31].

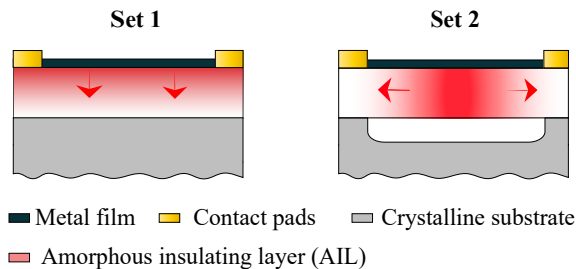


Figure 1. Sample configurations. The gradient of red represents the distribution of T_{ph} , and red arrows show the direction of heat flow. Set 1 (left): the metal film is deposited on the amorphous insulating layer. Set 2 (right): the metal film and the amorphous insulating layer are suspended relative to the bulk substrate.

Here we focus on the study of the role of a silicon-based AIL in thermal transport in thin-film devices at low temperatures. Ballistic and diffusive regimes of phonon transport are expected to produce two different scenarios of heat dissipation from a metal film into the substrate. In the ballistic regime, when the scattering happens only at the interface, we deal with the thermal interface resistance, which corresponds to a $Z_K \propto T_{ph}^{-3}$ dependence [32], where Z_K is the Kapitza resistance and T_{ph} is the phonon temperature of the metal film. In the diffusive regime, the thermal resistance is determined by the AIL and can be expressed as $Z(T) \propto l_{AIL}/\kappa_{AIL}(T)$, where κ_{AIL} is the thermal conductivity of the AIL and l_{AIL} is the effective length of the amorphous insulator. In that case, $Z(T)$ is determined by the temperature dependence of $\kappa_{AIL}(T)$. To discriminate between these two possibilities, we prepare two different sets of samples, deposited on an AIL (see Figure 1). In set 1, we vary the film material and film thickness. In set 2, a thin metal film is deposited on the AIL, which is suspended above the crystalline substrate. The latter configuration allows

us to vary l_{AIL} without changing the material batch. Our main result is that the heat dissipation in both sets is controlled by the thickness of the AIL, l_{AIL} , and is described by the $Z(T) \propto T^{-1}$ dependence. The data are quantitatively consistent with $\kappa_{AIL}(T) \propto T$ observed in independent calorimetric measurements [24, 33]. Our finding also demonstrates the insignificant role of the Kapitza resistance at $T > 5$ K.

II. DEVICES AND METHODS

Set 1 includes films of various metals deposited on commercial substrates based on an amorphous silicon dioxide (SiO_2) layer on the top of silicon (Si). The thickness of SiO_2 , considered here as the AIL, is about 300 nm, and the thickness of the Si substrate is 400 μm . Set 2 includes a thin NbN metallic layer deposited on a multilayer ($\text{SiN}_x\text{:H/SiO}_2\text{/GaAs}$) substrate. The thickness of $\text{SiN}_x\text{:H/SiO}_2$, considered here as the AIL, is about 700 nm. See Appendix A for details. Although the substrates come from different suppliers, we see no difference in the experimental results.

To study the heat dissipation law, we investigate a change of T_e as a function of Joule power per unit area of the metal film (P_{2D}). To measure T_e we use resistive thermometry for the Au/Ni sample and noise thermometry for all other samples. For resistive thermometry, we measure the current-voltage ($I - V$) characteristic, and define T_e from the resistance $R(T_e) = V/I$ and the $R(T)$ dependence obtained at low bias current. For noise thermometry, we measure the current noise spectral density S_I in the current-biased regime and determine the noise temperature as $T_N = S_I (dV/dI) / 4k_B$. The length of our samples (L) is chosen to be much longer than the electron-phonon length l_{e-ph} (see Appendix B), which allows us to ignore the electronic contribution to the heat outflow. The configuration also implies uniformity of T_e along the length L in set 1, and, as a consequence, $T_N = T_e$. The situation in set 2 is different. Since the temperature gradient is established along the length L in the suspended bridges (see Figure 1), T_N reflects the length-averaged temperature.

It is instructive to estimate the approximate size of the effective thermal conductances $G \equiv dP_{2D}/dT_e$ at $T = 5$ K expected for different cooling mechanisms. The Joule heat can be removed from the metal film by thermal conduction and thermal radiation. For set 1, the thermal conduction occurs through the metal film, the AIL, and the bath, connected in series. Here the total G can be defined by the smallest contribution among the electron-phonon conductance $G \approx (0.74 - 30) \times 10^5 \text{ WK}^{-1}\text{m}^{-2}$ (see Appendix B), the Kapitza thermal conductance $G \approx (1.15 - 1.5) \times 10^5 \text{ WK}^{-1}\text{m}^{-2}$ (see Appendix C), and the thermal conductance due to diffuson lattice excitations of the substrate. The latter thermal conductivity can be

calculated as $G = \kappa_{AIL}/l_{AIL} \approx 3 \times 10^5 \text{ WK}^{-1}\text{m}^{-2}$ for $l_{AIL} = 300 \text{ nm}$ and $\kappa_{AIL} \approx 0.09 \text{ W/Km}$ for amorphous silica [24]. At 5 K all terms are of the same order of magnitude. At increasing T , the thermal relaxation will be governed by the term with the weakest temperature dependence. As we show below, it is the thermal conductance of the AIL that determines $G \propto T$ in the range from 5 to 70 K. For set 2, the thermal conduction occurs from the metal film and the AIL to the metal contacts, which represent the thermal bath in this case. Here the thermal conductance is given by $G \approx \kappa_x/\alpha L^2$, where $\alpha = \pi^2/64$. In the present experiment $\kappa_x = \kappa d + \kappa_{AIL}d_{AIL}$, where κ is the thermal conductivity of the film and d_{AIL} is the thickness of the AIL (see Sec. III for details). In that case, the total G is determined by the largest contribution to the two-dimensional (2D) thermal conductivity κ_x related to electrons and phonons in the film or phonons in the AIL. A preliminary estimate of the thermal conductance due to the AIL is $G \approx 180 \text{ WK}^{-1}\text{m}^{-2}$ for $l_{AIL} = 50 \mu\text{m}$. To estimate G of the film, we suppose that electron and phonon contributions to κ_x are of the same order. The thermal conductance of electrons determined according to the Wiedemann–Franz law yields $G \approx 0.4 \text{ WK}^{-1}\text{m}^{-2}$ for $L = 50 \mu\text{m}$. Thus, in suspended devices, due to $d_{AIL}/d \gg 1$, the thermal conductance of the amorphous substrate is expected to dominate already at $T=5 \text{ K}$. Finally, electromagnetic thermal radiation provides the least-effective channel for cooling ($G = 4\sigma T^3 \approx 2.8 \times 10^{-5} \text{ WK}^{-1}\text{m}^{-2}$ at 5 K according to the Stefan–Boltzmann law, where σ is the Stefan–Boltzmann constant), and we do not consider it further.

III. RESULTS

Set 1

Here we investigate metal films based on various materials (NbN, InO_x, and Au/Ni) deposited on similar SiO₂/Si substrates. Images of the samples and schematic sketches of the thermometry methods are presented in Figure 2(a-c): see Appendix A for details. The materials substantially differ in the level of disorder, the resistivity varies by 3 orders of magnitude, and the film thickness d varies in the range from 5 to 130 nm. Figure 2(d) shows the measured T_e as a function of P_{2D} on a log-log scale. In the limit of small heating, T_e remains close to the bath temperature T_b , which corresponds to the plateau in the $T_N(P_{2D})$ -dependence. Note that T_b is sample specific. For superconducting NbN and InO_x films, T_b is chosen to be slightly higher than the critical temperature of the superconducting transition to keep samples in the normal state. For the nonsuperconducting Au/Ni device, $T_b = 0.5 \text{ K}$; however, $T < 15 \text{ K}$ data were omitted due to the lack of accuracy of resistive ther-

metry in this temperature range. With intense heating, when $T_e \gg T_b$ regime is achieved, we observe the same power-dependency for all samples characterized by the power-law dependence $P_{2D} \propto T_e^2$ (the dashed guideline). Overall, the measured $T_e(P_{2D})$ -dependence can be fitted by the equation $P_{2D} = \Sigma^{2D}(T_e^n - T_b^n)$ (solid lines), where Σ^{2D} is the two dimensional cooling rate and $n = 2$ is the exponent in heat-outflow law. The fact that a similar dependence is observed for different materials clearly indicates that the observed effect is mediated by the substrate.

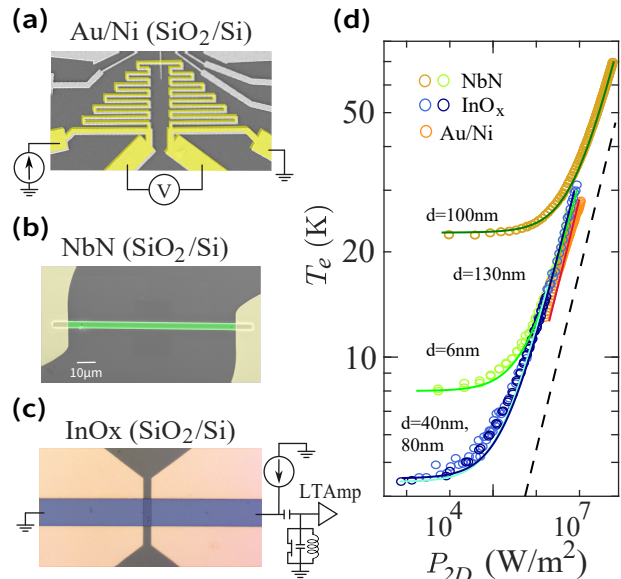


Figure 2. Devices and the experimental methods. The photographs from scanning electron and optical microscopes of a few samples with schematic sketches of the experiment: resistive thermometry, applied for the Au/Ni device (a), and noise thermometry, utilized for NbN device (b) and InO_x device (c). (d) The measured T_e is presented as a function of P_{2D} on a log-log scale for samples with various metal-film thicknesses d . The solid lines represent the fits, obtained with the expression $P_{2D} = \Sigma^{2D}(T_e^n - T_b^n)$ with the power index $n = 2$. The dashed black line displays $P_{2D} \propto T_e^2$ as a guide for the eye.

In Figure 3 we plot the fit parameter Σ^{2D} versus the film thickness d . Here we add the series of data for NbN samples with d varying by 2 orders of magnitude, each symbol on a graph corresponding to an individual sample. Σ^{2D} remains insensitive to d and is close to $\Sigma_{av}^{2D} = 10^4 \text{ W K}^{-2}\text{m}^{-2}$ for all samples studied (the dashed green line). In addition, we compare our data with three-dimensional (3D) heat dissipation, which is defined as $IV/\Omega = \Sigma_{3D}(T_e^n - T_b^n)$, where Ω is the sample volume and $\Sigma_{3D} \approx \text{const}$. The dashed orange line shows the trend expected for 3D heat dissipation, which does not occur here. Summarizing the experimental results from Figure 2 and Figure 3 our main findings are $P_{2D} \propto T_e^2$ and $\Sigma^{2D} \approx \text{const}$. The temperature de-

pendence of P_{2D} we find is in contradiction with the model of thermal boundary resistance, which implies that the heat flow is due to ballistic phonons and predicts $P_{2D} \propto T_{ph}^4$. In the inset Figure 3, we compare typical experimental values of the thermal resistance, defined as $Z = 1/n\Sigma_{av}^{2D}T^{n-1}$, with the expected Kapitza thermal resistance Z_K . Here Z_K is calculated in the frame of the acoustic mismatch model (AMM) [32]. The red line shows estimations for the interfaces between all metallic films and the SiO₂ layer (see Appendix C for details). From the graph, we find $Z > Z_K$ at $T > 5$ K, which indicates a gross violation of ballistic phonon flight in this temperature range. This observation demonstrates that in this temperature range the probability of a phonon backscattering approaches unity.

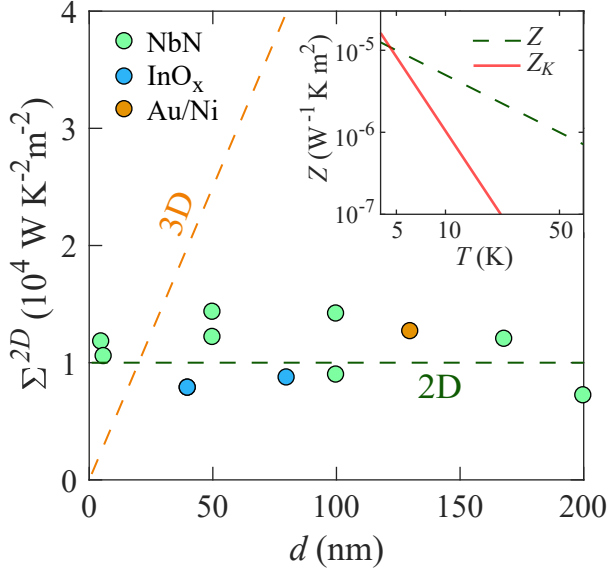


Figure 3. The thickness dependencies of the experimental 2D cooling rate Σ^{2D} . The symbols represent Σ^{2D} for different materials (NbN, InO_x, Au/Ni) deposited on a SiO₂/Si substrate. The dashed green and orange lines highlight 2D and 3D heat dissipation. The inset shows the temperature dependencies of the thermal resistance Z and the Kapitza resistance Z_K (red line) on a log-log scale.

To gain further understanding of the $P_{2D} \propto T_e^2$ dependence we consider that the measured heat-dissipation dependence is restricted by the diffusive heat propagation in the AIL. It is convenient to introduce a gradient of the phonon temperature T_{ph} across the AIL (see the inset in Figure 4). The boundary conditions at the upper and bottom surfaces of the AIL are $T_{ph}(z=0) = T_e$ and $T_{ph}(z=d_{AIL}) \simeq T_b$. Here we ignore the contribution of the crystalline Si substrate since its thermal resistance is 3 orders of magnitude lower than the thermal resistance of the AIL (see Appendix E for details). The heat-flux

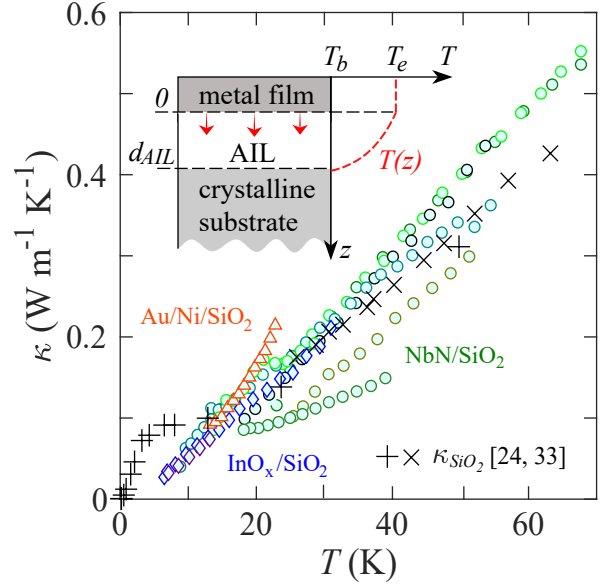


Figure 4. Comparison of thermal conductivity derived from differential thermal resistance with the data from calorimetric measurements. The colored symbols correspond to the thermal conductivity of the AIL calculated with Eq.(2) for NbN/SiO₂, InO_x/SiO₂, and Au/Ni/SiO₂ devices. The black symbols represent the data for SiO₂ thermal conductivity (κ_{SiO_2}) obtained with calorimetric measurements [24, 33]. The inset shows the thermal relaxation in a metal film deposited on the substrate with the AIL leads to a temperature gradient across the AIL in the z -direction.

continuity condition is given by the expression

$$\frac{d}{dz} \left(\kappa_{AIL} \frac{dT_{ph}(z)}{dz} \right) = 0 \quad (1)$$

where κ_{AIL} is the thermal conductivity of the AIL. The solution of Eq.(1), described in Appendix D, connects $\kappa_{AIL}(T_e)$ and the thermal resistance $Z \equiv dT_e/dP_{2D}$. Note that κ_{AIL} also depends on T_{ph} at the z -axis coordinate. Thus, under the assumption of a substrate effect, one obtains the temperature dependence of κ_{AIL} :

$$\kappa_{AIL}(T_e) = \frac{d_{AIL}}{Z} \quad (2)$$

The differential thermal resistance Z yields a nearly linear temperature dependence of κ_{AIL} under the assumption of the substrate effect. Figure 4 shows κ_{AIL} obtained via Eq.(2) as a function of T on a linear scale. Colored symbols correspond to κ_{AIL} obtained for all samples. For comparison, we plot the values of the thermal conductivity of SiO₂ (κ_{SiO_2}) obtained by calorimetry [24, 33]. The measured κ_{AIL} is in good agreement with the calorimetric data κ_{SiO_2} over the temperature range from 20 to 70 K. In the range from 4 to 20 K our estimation of κ_{AIL} deviates from κ_{SiO_2} , and the origin of the discrepancy is unclear. In the next section, we verify

the functional dependence of Z on the length of the AIL in suspended devices.

Set 2

As follows from Eq. (2), for unequivocal identification of the AIL bottleneck mechanism a variation of the amorphous-layer thickness is desirable. To this end, we perform analogous experiments in metal-on-AIL bridges suspended in a vacuum above the crystalline substrate. The idea is that the Joule heat released in the metal film propagates along the bridge toward the massive Ohmic contacts [see Figure 5 (a)] so that the thermal gradient is directed along the bridge and its length L controls the solution of the heat-balance equation. Using 5-nm-thick NbN films deposited on 700-nm-thick AIL, we ensure that the thermal relaxation is determined by the thermal properties of the AIL. In this experiment, the AIL consists of two layers of amorphous insulators: 200-nm-thick SiN_x:H and 500-nm-thick SiO₂ layers. We also fabricate two nonsuspended devices on the same substrate (see Table II in Appendix A for detailed information). A schematic illustration of sample set 2 and the thermal gradients is given in Figure 5 (a) for suspended (a1, a2) and nonsuspended (b1, b2) devices.

Assuming that the phonon temperature is uniform within the cross section of the bridge and $T_e = T_{ph} = T$ we obtain a thermal-balance equation for a suspended device:

$$\frac{\partial}{\partial x} \left(\kappa_x \frac{\partial T}{\partial x} \right) = -P_{2D}, \quad (3)$$

where κ_x is the total (two-dimensional) thermal conductivity of the bridge and x is the coordinate along the bridge. In Figure 5 (b) we plot the measured noise temperature T_N for all four devices from set 2 as a function of P_{2D} . We observe the same power-law functional dependence as before, $P_{2D} \propto (T_N^2 - T_b^2)$, with a notable distinction. Here the suspended devices a1 and a2 exhibit strong length dependence: the longer device a2 is much easier to heat up. This effect is not observable for devices b1 and b2 lying on the substrate, and it is similar to the data for set 1 discussed above. The observed length dependence is consistent with the fact that the solution of Eq. (3) in the reduced coordinate $\tilde{x} \equiv x/L$ is a universal function of length $T^2(\tilde{x}) \propto L^2 P_{2D}$ at $T \gg T_b$. This is illustrated in Figure 5 (c), which shows the thermal resistance $Z = dT_N/dP_{2D}$ evaluated at $T_N = 25$ K as a function of L . The data for suspended devices are indeed consistent with $Z \propto L^2$ (see the dashed line), whereas $Z \approx \text{const}$ is observed for the nonsuspended devices (see the dotted line).

The observation of a parabolic temperature dependence $P_{2D} \propto (T_N^2 - T_b^2)$ is consistent with a linear temperature dependence $\kappa_x \propto T$ of the heat conductivity

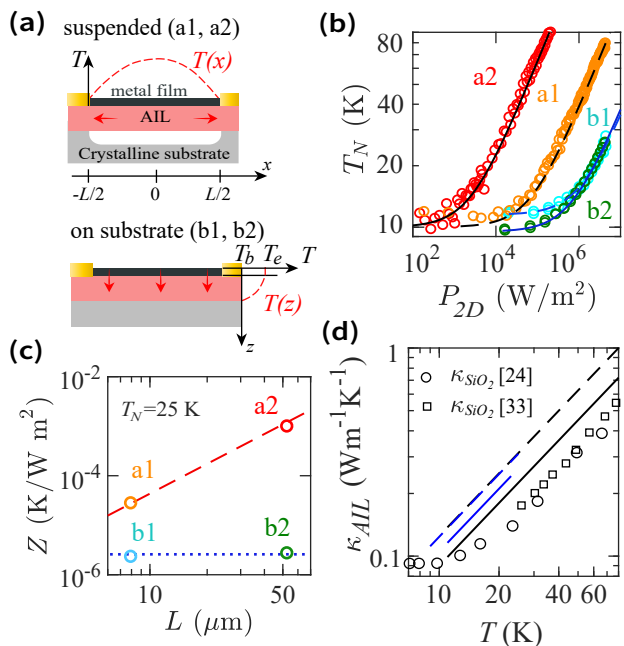


Figure 5. Comparison of heat transport in the suspended NbN and NbN devices on the substrate. (a) Schematics of the relevant mechanisms of the thermal transport of suspended samples (a1 and a2) and samples on the substrate (b1 and b2). (b) T_N as a function of P_{2D} on a log-log scale at the bath temperature $T_b \approx 10$ K. The data for samples a1 and a2 are displayed with orange and red symbols, while the data for samples b1 and b2 are displayed with blue and green symbols. The solid and dashed black lines represent the fits of the data for samples a1 and a2 with T_N (see the main text). The solid and dashed blue lines represent the fits of the data for samples b1 and b2 with $T_N = \sqrt{(P_{2D})/\Sigma^{2D} + T_b^2}$. (c) The thermal resistance Z versus length L of the samples L at $T_N = 25$ K on a log-log scale. (d) The calculated thermal conductivity of the AIL for the studied NbN samples in comparison with κ_{SiO_2} . Solid and dashed black lines correspond to the values of κ_{AIL} , estimated with Eq. (3), for samples a1 and a2. The blue lines correspond to κ_{AIL} obtained with Eq.(2), for NbN samples b1 and b2. The symbols demonstrate the data for κ_{SiO_2} [24, 33].

in Eq. (3). This yields the estimation of the thermal resistance $Z = \pi^2 L^2 / 64 \kappa_x$. In the present experiment $\kappa_x = \kappa_{\text{NbN}} d_{\text{NbN}} + \kappa_{\text{AIL}} d_{\text{AIL}}$, where κ_{NbN} is the thermal conductivities of NbN (electron and lattice). In our devices with $d_{\text{AIL}} \gg d_{\text{NbN}}$, the contribution of the NbN film is negligible and we obtain $\kappa_x \approx \kappa_{\text{AIL}} d_{\text{AIL}}$, also consistent with an independent estimate of κ_{NbN} . Solving Eq. (3) for suspended devices, we fit the data from Figure 5 (b) and extract the corresponding κ_{AIL} . In this two-step procedure we find a temperature profile along the bridge $T^2(\tilde{x}) = T_b^2 + (T_{\text{max}}^2 - T_b^2) (1 - 4\tilde{x}^2)$, where $|\tilde{x}| \leq 1/2$, and subsequently evaluate the noise temperature of the device $T_N = \int T(\tilde{x}) d\tilde{x}$. The data for nonsuspended devices are analysed according to Eq. (2) in the same manner as set 1 before. Figure 5 (d) shows the

obtained linear dependencies of κ_{AIL} on temperature for all four devices, with the same line styles as the fits in Figure 5 (b). Note that the temperature ranges, which vary for the samples, correspond to the range of T_N variation in the experiment. Because of the lack of data on the calorimetric measurement of the thermal conductivity of amorphous $\text{SiN}_x\text{:H}$ we compare our results with data for SiO_2 only. The data are consistent with each other within the uncertainty of about 15%, as well as with independent calorimetric measurements of κ_{SiO_2} , shown by symbols. The plotted data of κ_{SiO_2} are the same as in Figure 4 in other temperature range. In the range from 10 to 60 K, our estimation of κ_{AIL} for set 2 slightly deviates from κ_{AIL} for set 1. The origin of the discrepancy can be explained by the uncertainty in the thermal conductivity of $\text{SiN}_x\text{:H}$, which is expected to exceed the thermal conductivity of SiO_2 .

IV. DISCUSSION

We now summarize and discuss our observations of thermal transport in the samples studied. The observed heat flow rate with the exponent $n = 2$ is not compatible with the electron-phonon relaxation or the phonon relaxation mediated by the Kapitza thermal resistance [8]. Experimental findings such as (i) the similar value of Σ_{2D} observed for the different metal films and (ii) the functional dependence of Z on the length of the AIL strongly indicate that the heat transport is mediated by the thermal properties of the AIL. This effect is also confirmed by the obtained dependence $\kappa_{AIL} \propto T$.

Heat transfer in an AIL is different from heat transfer in a crystalline material, and l_{ph} in amorphous solids strongly decreases with increasing T . In silicon-based materials at a certain temperature, l_{ph} reaches the Ioffe-Regel criterion. Note that the phonons, considered as plane waves with well-defined wave vector q and frequency ω , are in a strongly scattering regime and cannot propagate and transfer heat here [25]. By contrast, the heat transfer is expected to be controlled by diffusons [23, 25–27]. In this framework, the thermal conductivity is determined by $\kappa_{AIL} \propto \int g(\omega)D(\omega)C(\omega/T)d\omega$, where $g(\omega)$ and $D(\omega)$ are the density and diffusivity of vibrational modes, respectively, and $C(\omega/T) = x^2/\sinh^2 x$ with $x = \hbar\omega/2k_B T$, is the specific heat capacity of a harmonic oscillator. For diffusons, the functions $g(\omega)$ and $D(\omega)$ are approximately constant in some frequency interval [23, 26], which leads to $\kappa \propto k_B^2 T/(\hbar a_0)$ in given temperature range, where a_0 corresponds to an interatomic distance. In our study, the Ioffe-Regel threshold is expected to occur at approximately 10 K [23, 34]. The estimated phonon wavelength λ and phonon mean free path $l_{ph}(\omega)$ at 10 K are 9 nm and approximately 4.5 nm, respectively. However, in our experiment we do not observe the plateau of κ , which has been found with calorimetric measurements [33] in the range from 5 to 20 K (see Figure 4). The position of this plateau in $\kappa(T)$ agrees with the position of the boson peak in vitreous SiO_2 [27, 35], and is usually considered as the boundary between ballistic and diffusely propagating lattice excitations. It is possible that the fact that we do not observe a plateau is related to the fabrication process for contemporary commercial substrate materials, and this remains to be clarified in future experiments.

Our results also shed light on a recent proposal of a universal energy-relaxation bottleneck in thick strongly disordered metallic films [36]. In this work, since $\Sigma_{2D} \approx \text{const}$ in Figure 3, we do not observe an impact of phonon scattering in NbN films on heat transfer up to thicknesses on the order of 200 nm. Further studies of disordered metal films on crystalline substrates are required to verify the strong phonon-scattering effects inherent in disordered metal films. Our results may also be useful for interpreting the thermal transport in devices embedded in an AIL at low temperatures. At subkelvin temperatures, when the phonon mean free path is long enough, the exponent in the heat flow rate n is determined by the internal properties of the metal film [37]. Thus, the decrease of n at low T in other devices on amorphous dielectric substrates [21] may be related to the transition from the electron-phonon coupling regime to the substrate effect. In addition, the AIL may be a possible candidate for phonon-filtering applications [38], since l_{ph} in amorphous insulators is frequency dependent ($l_{ph} \propto \omega^{-4}$ [23, 39]). In this respect, the phonon scattering in amorphous insulators resembles phonon propagation as a low-pass energy filter, and the low-energy modes have an opportunity to propagate, while the high-energy phonons cannot pass. The energy filtration can be an intriguing alternative to the models of strong acoustic mismatch, which assume ballistic phonon filtering at the interface depending on the angle of incidence [16].

V. CONCLUSION

In conclusion, we conduct a systematic study of the electronic heat flow rate in metal films on silicon-based amorphous insulating substrates at temperatures above 5 K. For samples lying on the substrate, the observed two-dimensional heat-relaxation independence with $P_{2D} = \Sigma^{2D}(T_e^n - T_b^n)$ with exponent $n \simeq 2$ is inconsistent with both electron-phonon cooling and Kapitza resistance. For samples suspended above the crystalline substrate, we observe length-dependent heat relaxation with the same exponent. This effect is quantitatively explained by the low thermal conductance of the amorphous insulating layer. The exponent $n \simeq 2$ is related to the well-known linear temperature dependence of thermal conductivity in amorphous solids, which is described by the concept of diffuson lattice excitations. Our findings refine the un-

derstanding of thermal transport in mesoscopic devices embedded in an amorphous dielectric.

ACKNOWLEDGEMENTS

We are grateful to E.S. Tikhonov for fruitful discussions and help in the initial stage of this work. We thank A.O. Denisov for sharing experimental results for Au/Ni sample. We are grateful to M. Rocci for fabrication of Au/Ni devices as a part of a different project. The transport and noise measurements were funded by the Russian Science Foundation (Project No. 19-72-10101). The theoretical analysis was supported by the Council on grants of the President of the Russian Federation (No. MK-1308.2019.2). Resistive thermometry was performed under the state task of the ISSP RAS.

Note added.—Recently we have become aware of Ref. [40], which provides insights about the presence of diffusivelike damping of vibrational excitations in amorphous materials and even ordered crystals, and its strong influence on low-T properties of solids.

APPENDIX A: DETAILS OF SAMPLE FABRICATION AND EXPERIMENTAL SETUP

The films of set 1 are deposited on a SiO₂/Si substrate obtained from NOVA Electronic Materials LLC. The 280-300-nm SiO₂ layer is produced by the thermal oxidation of a crystalline Si substrate.

The Au(120 nm)/Ni(10 nm) bilayer is deposited by means of electron-beam lithography and the lift-off technology [21]. Here we use the residual resistance ratio, $r_R = (R_{300K} - R_{20K})/R_{20K}$, to characterize the metal films. Positive values of r_R correspond to $dR(T)/dT > 0$, and vice versa. The bilayer is characterized by $r_R = 2$ and resistivity $\rho = 1.6 \times 10^{-8} \Omega \text{ m}$ at 10 K.

The NbN films of set 1 are deposited on a substrate at room temperature with dc magnetron sputtering. The NbN films have $r_R = -0.3$, $\rho = 10^{-5} \Omega \text{ m}$ at 20 K, and critical temperature of the superconducting transition $T_c = 13.5 \text{ K}$ in 200-nm-thick film. The Ti(5 nm)/Au(200 nm) metal pads to NbN are fabricated with standard photolithography and thermal evaporation.

The amorphous InO_x films are characterized by $r_R = -0.3$, $\rho = 8 \times 10^{-5} \Omega \text{ m}$ at 4 K, and $T_c = 2.7 \text{ K}$. The metal Ti/Au leads are formed on the substrate before evaporation of InO_x films from In₂O₃ granules at room temperature [41].

All films are patterned into a bridge or a meander by a plasma-chemical etching or lift-off. Photographs of samples are presented in Figure 2(a), and the sizes and resistance of the samples are presented in (Table I).

Table I. Parameters of set 1. d is the thickness, w the width, L the length and R the resistance measured above T_c for superconducting NbN and InO_x films or at 10K for Au/Ni bilayer.

Sample	d (nm)	w (μm)	L (μm)	R ($k\Omega$)
NbN	5	0.66	12.3	129
	6	10.3	10.2	1.75
	50	0.55	12.6	4.23
		0.97	25.8	5.16
	100	0.54	12.9	2.5
	168	0.95	25.6	2.68
	200	3.3	93	1.44
InO _x	40	1	22.5	1.76
	80	3.7	3.1	1.66
Au/Ni	130	10.3	9.2	1.02
Au/Ni	130	0.25	105	0.03

The 5-nm NbN film of set 2 is deposited on a SiN_x:H/SiO₂/GaAs substrate at 250°C with dc magnetron sputtering. The SiO₂ layer is grown on a crystalline GaAs substrate by chemical vapor deposition (CVD) and the SiN_x:H layer is grown by plasma-enhanced chemical vapor deposition (PECVD) at 250°C [42]. The thicknesses of AIL SiN_x:H and SiO₂ membranes are 200 and 500 nm, respectively. The NbN film has $r_R = -0.25$ and resistivity ρ of about $= 4 \times 10^{-6} \Omega \text{ m}$ at 10 K. ρ of NbN in set 2 is 2 times smaller than in set 1 due to the higher temperature of deposition. The NbN film is patterned to form a bridge-type structure with Ti/Au metal pads. To fabricate the suspended structure (membrane), beyond the NbN bridge, SiN_x:H and SiO₂ layers are dissolved in hydrofluoric acid, and GaAs under the membrane is etched in a solution of hydrogen peroxide, ammonia, and water.

Table II. Parameters of set 2. d is the thickness, w the width, L the length and R the resistance measured above T_c for superconducting NbN films.

Sample	d (nm)	w (μm)	L (μm)	R ($k\Omega$)
b1	5	6.5	8.7	4.1
b2	5	6.35	50	13
a1	5	3.1	7	1.6
a2	5	3.77	53.8	7.2

The noise and resistance measurements are performed in a homemade ⁴He insert, inside which the samples are in a vacuum. For noise thermometry, the current-noise spectral density is measured with a resonant tank circuit at the input of a homemade low-noise amplifier (LTAMP) with a gain of about 6 dB, input current noise of approximately $10^{-27} \text{ A}^2/\text{Hz}$ and dissipated power of approximately $250 \mu\text{W}$ (see the sketch in Figure 2(c)). The output noise signal of the LTAMP is amplified by a cascade of low-noise amplifiers with a gain of 75 dB in total, and

then it is passed through a system of band-pass filters and measured by a power detector. The current dependence of the power is averaged over several measurements to reduce random error, and the uncertainty of the measured temperature is within 0.4 K. Calibration is achieved with equilibrium Johnson-Nyquist noise thermometry. For this purpose, we use a commercial high-electron-mobility transistor connected in parallel with the device, which is depleted otherwise. At high sample resistance (above $1k\Omega$), the setup has a bandwidth Δf of approximately 1 MHz around a center frequency of 40 MHz. The low-quality factor of the resonant tank circuit precludes the use of noise thermometry in the Au/Ni device, which has a resistance of about 30Ω . For the Au/Ni device the electron temperature is measured by resistive thermometry as an alternative [see the sketch of setup in Figure 2(a)]. Since the accuracy of resistive thermometry crucially depends on the function dR/dT , we leave only data that provide the uncertainty of the measured temperature within 0.15 K. Our results obtained by resistive thermometry are qualitatively consistent with the data from local noise thermometry in the same material performed in the work reported in Ref. [21]. The relaxation rates smaller by a factor of 3 – 4 obtained in Ref. [21] may result from the substrate overheating effect, which was not anticipated in that work.

APPENDIX B: ESTIMATION OF THE ELECTRON-PHONON COOLING

The electron-phonon length l_{e-ph} can be calculated as $l_{e-ph} = \sqrt{\mathcal{L}/\rho n \Sigma_{e-ph} T^{n-2}}$ or $l_{e-ph} = \sqrt{\tau_{e-ph} D}$, where Σ_{e-ph} and τ_{e-ph} are the electron-phonon coupling constant and the electron-phonon relaxation time, n is the exponent, D is the diffusion coefficient, and \mathcal{L} is the Lorentz number. Using $\Sigma_{e-ph} = 7.7 \times 10^9 \text{ WK}^{-n} \text{ m}^{-3}$, $n = 5.07$, for Au [43], $\Sigma_{e-ph} = 1.85 \times 10^9 \text{ WK}^{-n} \text{ m}^{-3}$, $n = 6$, for InO_x [44], and the value of τ_{e-ph} extrapolated to 10 K ($\tau_{e-ph} = 9 \text{ ps}$) and $D = 0.3 \text{ cm}^2/\text{s}$ for NbN [45] we calculate l_{e-ph} is 350 nm for Au, 18 nm for NbN at 10 K, and 6.6 nm for InO_x at 5 K. The effective thermal conductance $G = dP_{2D}/dT_e$ is given by $G = n \Sigma_{e-ph} T^{n-1} d$ or $G = C_e \tau_{eph}^{-1} d$, where d is the film thickness, C_e is the electron specific heat capacity.

APPENDIX C: ESTIMATION OF KAPITZA RESISTANCE

The Kapitza resistance in analogy to the Stefan-Boltzmann law is described by the heat-dissipation cooling law $P = \Sigma_K A (T_{ph}^4 - T_b^4)$, where Σ_K is the cooling rate due to Kapitza resistance. Σ_K can be estimated with AMM or diffuse mismatch model (DMM). The AMM

describes phonon propagation through the interface between two media in analogy to Snell's law for electromagnetic waves. The probability of phonon transmission depends on the angle of the incident phonon related to the critical angle, where the critical angle is determined by the acoustic properties of the medium [46]. In the DMM the diffusive scattering of phonons at the interface is taken into account, and thus the phonon transmission probability depends only on the phonon densities of the states and sound velocities of the two media [32]. In the DMM Σ_K between the film phonons and the substrate phonons can be obtained by summing over the two transverse acoustic modes and one longitudinal acoustic mode [32]:

$$\Sigma_K = \frac{\pi^2 k_B^4}{120 \hbar^3} \left(\frac{\frac{1}{v_{1L}^2} + \frac{2}{v_{1T}^2}}{\frac{1}{v_{1L}^2} + \frac{2}{v_{1T}^2} + \frac{1}{v_{2L}^2} + \frac{2}{v_{2T}^2}} \right) \left(\frac{1}{v_{2L}^2} + \frac{2}{v_{2T}^2} \right) \quad (4)$$

where v_{iL} and v_{iT} are the longitudinal and transverse sound velocities in medium i . In the case of solid-solid boundaries, the DMM and the AMM give similar predictions. For simplicity, we use the DMM for estimation of the Kapitza resistance. To calculate Σ_K , we use the values of the sound velocity reported for Ni [32], amorphous SiO_2 [47], and the cubic phase of NbN [48]. v_L and v_T in InO_x are obtained from elastic constants and the density of In_2O_3 [49, 50]. We find that Σ_K covers the range from 230 to $300 \text{ W K}^{-4} \text{ m}^{-2}$ for the thermal contacts of NbN- SiO_2 , Ni- SiO_2 , and In_2O_3 - SiO_2 . The thermal impedance mediated by the Kapitza resistance Z_K can be calculated as $Z_K = 1/G$, where the effective thermal conductance $G = 4 \Sigma_K T^3$. The temperature dependence of Z_K for all interfaces is shown in the inset in Figure 3.

APPENDIX D: DERIVATION OF THERMAL CONDUCTIVITY

Integrating the expression for the heat flow

$$P_{2D} = \kappa_{AIL} \frac{dT_{ph}}{dz} = \text{const}(z) \quad (5)$$

over the thickness of the AIL layer, one gets

$$P_{2D} d_{AIL} = \int_0^{d_{AIL}} \kappa_{AIL} \frac{dT_{ph}}{dz} dz = \int_{T_b}^{T_e} \kappa_{AIL} dT_{ph}, \quad (6)$$

which, after differentiation over the electron temperature, yields

$$\frac{dP_{2D}}{dT_e} d_{AIL} = \frac{d}{dT_e} \int_{T_b}^{T_e} \kappa_{AIL} dT_{ph} = \kappa_{AIL}(T_e), \quad (7)$$

that is, Eq. 2.

APPENDIX E: ESTIMATION OF SiO₂ AND Si BOTTLENECKS

In the main text, the thermal resistance Z of the substrate is determined as $Z \equiv dT_e/dP_{2D}$. The substrate used in set 1 is made of an amorphous SiO₂ layer on bulk crystalline Si with thicknesses of d_{AIL} and d_{Si} , respectively. Since the geometry of the metal films satisfies the conditions $w, L > d_{AIL}$ and $w, L < d_{Si}$, a one-dimensional heat outflow into the AIL and a further three-dimensional heat outflow into the Si substrate are expected [51]. The thermal resistances mediated by the AIL and the silicon substrate (Z_{SiO_2} and Z_{Si}) can be calculated as $Z_{SiO_2} = d_{AIL}/\kappa_{SiO_2}$ (see the derivation in Appendix D and $Z_{Si} = \sqrt{Lw}/\kappa_{Si}$ [51]). Taking the thermal conductivities $\kappa_{SiO_2} \simeq 0.1 \text{ WK}^{-1}\text{m}^{-1}$ [24] and $\kappa_{Si} \simeq 10^4 \text{ WK}^{-1}\text{m}^{-1}$ at 10 K [52] and the maximum value of $w \times L = 307 \mu\text{m}^2$, we estimate $Z_{SiO_2} = 3 \times 10^{-6} \text{ W}^{-1}\text{Km}^2$ and $Z_{Si} = 10^{-9} \text{ W}^{-1}\text{Km}^2$ at 10 K.

-
- [1] W. Pernice, C. Schuck, O. Minaeva, M. Li, G. Goltsman, A. Sergienko, and H. Tang, “High-speed and high-efficiency travelling wave single-photon detectors embedded in nanophotonic circuits,” *Nat. Commun.* **3**, 1325 (2012).
- [2] V. Kovalyuk, W. Hartmann, O. Kahl, N. Kaurova, A. Korneev, G. Goltsman, and W. H. P. Pernice, “Absorption engineering of NbN nanowires deposited on silicon nitride nanophotonic circuits,” *Opt. Express* **21**, 22683 (2013).
- [3] R. Gourgues, I. E. Zadeh, A. W. Elshaari, G. Bulgarelli, J. W. N. Los, J. Zichi, D. Dalacu, P. J. Poole, S. N. Dorenbos, and V. Zwiller, “Controlled integration of selected detectors and emitters in photonic integrated circuits,” *Opt. Express* **27**, 3710 (2019).
- [4] K. S. Novoselov, A. K. Geim, S. V. Morozov, D. Jiang, Y. Zhang, S. V. Dubonos, I. V. Grigorieva, and A. A. Firsov, “Electric field effect in atomically thin carbon films,” *Science* **306**, 666–669 (2004).
- [5] M. Freitag, M. Steiner, Y. Martin, V. Perebeinos, Z. Chen, J. C. Tsang, and P. Avouris, “Energy dissipation in graphene field-effect transistors,” *Nano Lett.* **9**, 1883 (2009).
- [6] K. Smirnov, A. Divochiy, Y. Vakhtomin, P. Morozov, P. Zolotov, A. Antipov, and V. Seleznev, “NbN single-photon detectors with saturated dependence of quantum efficiency,” *Supercond. Sci. Technol.* **31**, 035011 (2018).
- [7] F. Marsili, V. B. Verma, J. A. Stern, S. Harrington, A. E. Lita, T. Gerrits, I. Vayshenker, B. Baek, M. D. Shaw, R. P. Mirin, and S. W. Nam, “Detecting single infrared photons with 93% system efficiency,” *Nat. Photonics* **7**, 210 (2013).
- [8] F. Giazotto, T. T. Heikkilä, A. Luukanen, A. M. Savin, and J. P. Pekola, “Opportunities for mesoscopies in thermometry and refrigeration: Physics and applications,” *Rev. Mod. Phys.* **78**, 217–274 (2006).
- [9] T. Lindström, J. E. Healey, M. S. Colclough, C. M. Muirhead, and A. Y. Tzalenchuk, “Properties of superconducting planar resonators at millikelvin temperatures,” *Phys. Rev. B* **80**, 132501 (2009).
- [10] O. Dupré, A. Benoit, M. Calvo, A. Catalano, J. Goupy, C. Hoarau, T. Klein, K. L. Calvez, B. Sacépé, A. Monfardini, and F. Levy-Bertrand, “Tunable sub-gap radiation detection with superconducting resonators,” *Supercond. Sci. Technol.* **30**, 045007 (2017).
- [11] S. Steinhauer, L. Yang, S. Gyger, T. Lettner, C. Errando-Herranz, K. D. Jöns, M. A. Baghban, K. Gallo, J. Zichi, and V. Zwiller, “NbTiN thin films for superconducting photon detectors on photonic and two-dimensional materials,” *Appl. Phys. Lett.* **116**, 171101 (2020).
- [12] A. M. Goldman and N. Marković, “Superconductor-insulator transitions in the two-dimensional limit,” *Phys. Today* **51**, 39 (1998).
- [13] B. Sacépé, M. Feigel’man, and T. M. Klapwijk, “Quantum breakdown of superconductivity in low-dimensional materials,” *Nat. Phys.* **16**, 734 (2020).
- [14] C. Müller, J. H. Cole, and J. Lisenfeld, “Towards understanding two-level-systems in amorphous solids: insights from quantum circuits,” *Rep. Prog. Phys.* **82**, 124501 (2019).
- [15] S. Cherednichenko, V. Drakinskiy, J. Baubert, J.-M. Krieg, B. Voronov, G. Goltsman, and V. Desmaris, “Gain bandwidth of NbN hot-electron bolometer terahertz mixers on 1.5 μm Si₃N₄/SiO₂ membranes,” *J. Appl. Phys.* **101**, 124508 (2007).
- [16] M. V. Sidorova, A. G. Kozorezov, A. V. Semenov, Y. P. Korneeva, M. Y. Mikhailov, A. Y. Devizenko, A. A. Korneev, G. M. Chulkova, and G. N. Goltsman, “Non-bolometric bottleneck in electron-phonon relaxation in ultrathin WSi films,” *Phys. Rev. B* **97**, 184512 (2018).
- [17] E. Baeva, M. Sidorova, A. Korneev, K. Smirnov, A. Divochiy, P. Morozov, P. Zolotov, Y. Vakhtomin, A. Semenov, T. Klapwijk, V. Khrapai, and G. Goltsman, “Thermal properties of NbN single-photon detectors,” *Phys. Rev. Applied* **10**, 064063 (2018).
- [18] S. B. Kaplan, “Acoustic matching of superconducting films to substrates,” *J. Low Temp. Phys.* **37**, 343 (1979).
- [19] W. Eisenmenger, K. Laßmann, H. J. Trumpp, and R. Krauß, “Quasiparticle recombination and 2Δ -phonon-trapping in superconducting tunneling junctions,” *Appl. Phys.* **11**, 307 (1976).
- [20] A. I. Bezuglyj and V. A. Shklovskij, “Kinetics of electron cooling in metal films at low temperatures and revision of the two-temperature model,” *J. Phys. Condens. Matter* **30**, 295001 (2018).
- [21] A. O. Denisov, E. S. Tikhonov, S. U. Piatrusha, I. N. Khrapach, F. Rossella, M. Rocci, L. Sorba, S. Roddaro, and V. S. Khrapai, “Strategy for accurate thermal biasing at the nanoscale,” *Nanotechnology* **31**, 324004 (2020).
- [22] W. A. Phillips, “Two-level states in glasses,” *Rep. Prog. Phys.* **50**, 1657 (1987).
- [23] Y. M. Beltukov, V. I. Kozub, and D. A. Parshin, “Ioffe-regel criterion and diffusion of vibrations in random lattices,” *Phys. Rev. B* **87**, 134203 (2013).
- [24] T. L. Smith, P. J. Anthony, and A. C. Anderson, “Effect of neutron irradiation on the density of low-energy excitations in vitreous silica,” *Phys. Rev. B* **17**, 4997–5008 (1978).
- [25] P. B. Allen, J. L. Feldman, J. Fabian, and F. Wooten, “Diffusons, locons and propagons: Character of atomic vibrations in amorphous Si,” *Philos. Mag. B* **79**, 1715 (1999).

- [26] N. Xu, V. Vitelli, M. Wyart, A. J. Liu, and S. R. Nagel, “Energy transport in jammed sphere packings,” *Phys. Rev. Lett.* **102**, 038001 (2009).
- [27] M. F. Ando, O. Benzine, Z. Pan, J.-L. Garden, K. Wondraczek, S. Grimm, K. Schuster, and L. Wondraczek, “Boson peak, heterogeneity and intermediate-range order in binary $\text{SiO}_2\text{-Al}_2\text{O}_3$ glasses,” *Sci. Rep.* **8**, 5394 (2018).
- [28] J. Yang, A. Kerman, E. Dauler, V. Anant, K. Rosfjord, and K. Berggren, “Modeling the electrical and thermal response of superconducting nanowire single-photon detectors,” *IEEE Trans. Appl. Supercond.* **17**, 581–585 (2007).
- [29] F. Marsili, F. Najafi, C. Herder, and K. K. Berggren, “Electrothermal simulation of superconducting nanowire avalanche photodetectors,” *Appl. Phys. Lett.* **98**, 093507 (2011).
- [30] J. P. Allmaras, A. G. Kozorezov, A. D. Beyer, F. Marsili, R. M. Briggs, and M. D. Shaw, “Thin-film thermal conductivity measurements using superconducting nanowires,” *J. Low Temp. Phys.* **193**, 380 (2018).
- [31] R. Baghdadi, J. P. Allmaras, B. A. Butters, A. E. Dane, S. Iqbal, A. N. McCaughan, E. A. Toomey, Q.-Y. Zhao, A. G. Kozorezov, and K. K. Berggren, “Multilayered heater nanocryotron: A superconducting-nanowire-based thermal switch,” *Phys. Rev. Applied* **14**, 054011 (2020).
- [32] E. T. Swartz and R. O. Pohl, “Thermal boundary resistance,” *Rev. Mod. Phys.* **61**, 605–668 (1989).
- [33] D. G. Cahill and R. O. Pohl, “Thermal conductivity of amorphous solids above the plateau,” *Phys. Rev. B* **35**, 4067–4073 (1987).
- [34] S. N. Taraskin and S. R. Elliott, “Ioffe-Regel crossover for plane-wave vibrational excitations in vitreous silica,” *Phys. Rev. B* **61**, 12031 (2000).
- [35] T. Nakayama, “Boson peak and terahertz frequency dynamics of vitreous silica,” *Rep. Prog. Phys.* **65**, 1195 (2002).
- [36] E. M. Baeva, N. A. Titova, A. I. Kardakova, S. U. Pitrusha, and V. S. Khrapai, “Universal bottleneck for thermal relaxation in disordered metallic films,” *JETP Lett.* **111**, 104 (2020).
- [37] J. M. Underwood, P. J. Lowell, G. C. O’Neil, and J. N. Ullom, “Insensitivity of sub-kelvin electron-phonon coupling to substrate properties,” *Phys. Rev. Lett.* **107**, 255504 (2011).
- [38] G. G. Melkonyan, H. Kröger, and A. M. Gulian, “Refrigerator with phonon filters: An application of the phonon deficit effect in superconducting tunnel junctions,” *J. Appl. Phys.* **94**, 4619 (2003).
- [39] P. Richet, *Encyclopedia of Glass Science, Technology, History, and Culture* (Wiley, New York, 2021).
- [40] M. Baggioli and A. Zaccone, “Universal origin of boson peak vibrational anomalies in ordered crystals and in amorphous materials,” *Phys. Rev. Lett.* **122**, 145501 (2019).
- [41] B. Sacépé, J. Seidemann, M. Ovadia, I. Tamir, D. Shahar, C. Chapelier, C. Strunk, and B. A. Piot, “High-field termination of a cooper-pair insulator,” *Phys. Rev. B* **91**, 220508 (2015).
- [42] V. I. Garmash, V. I. Egorkin, V. E. Zemlyakov, A. V. Kovalchuk, and S. Y. Shapoval, “A study of the effect of the structure of plasma-chemical silicon nitride on its masking properties,” *Semiconductors* **49**, 1727–1730 (2015).
- [43] O.-P. Saira, M. H. Matheny, L. Wang, J. Pekola, and M. Roukes, “Modification of electron-phonon coupling by micromachining and suspension,” *J. Appl. Phys.* **127**, 024307 (2020).
- [44] M. Ovadia, B. Sacépé, and D. Shahar, “Electron-phonon decoupling in disordered insulators,” *Phys. Rev. Lett.* **102**, 176802 (2009).
- [45] Y. P. Gousev, G. N. Goltsman, A. D. Semenov, E. M. Gershenzon, R. S. Nebosis, M. A. Heusinger, and K. F. Renk, “Broadband ultrafast superconducting NbN detector for electromagnetic radiation,” *J. Appl. Phys.* **75**, 3695 (1994).
- [46] W. A. Little, “The transport of heat between dissimilar solids at low temperatures,” *Can. J. Phys.* **37**, 334 (1959).
- [47] W. F. Love, “Low-temperature thermal brillouin scattering in fused silica and borosilicate glass,” *Phys. Rev. Lett.* **31**, 822–825 (1973).
- [48] D.-H. Ren and X.-L. Cheng, “First-principles calculations on the elastic and thermodynamic properties of NbN,” *Chin. Phys. B* **21**, 127103 (2012).
- [49] A. Walsh, C. R. A. Catlow, A. A. Sokol, and S. M. Woodley, “Physical properties, intrinsic defects, and phase stability of indium sesquioxide,” *Chem. Mater.* **21**, 4962 (2009).
- [50] K. Ellmer, “Resistivity of polycrystalline zinc oxide films: current status and physical limit,” *J. Phys. D* **34**, 3097 (2001).
- [51] E. Pop, “Energy dissipation and transport in nanoscale devices,” *Nano Res.* **3**, 147 (2010).
- [52] T. Ruf, R. Henn, M. Asen-Palmer, E. Gmelin, M. Cardona, H.-J. Pohl, G. Devyatych, and P. Sennikov, “Thermal conductivity of isotopically enriched silicon,” *Solid State Communications* **115**, 243–247 (2000).